Electronic Supplementary Information

NiMoFe/Cu nanowires core–shell catalyst for high-performance overall water splitting in neutral electrolytes

Xiaomin Cao,[a] Ronglei Fan,*[a,b] Ju Zhou,[a] Cong Chen,[a] Shunshun Xu,[a] Shuai Zou,[a] Wen Dong,[a] Xiaodong Su,[a] Sheng Ju[a] and Mingrong Shen*[a]

[a]*School of Physical Science and Technology, Jiangsu Key Laboratory of Thin Films, and Collaborative Innovation Center of Suzhou Nano Science and Technology, Soochow University, 1 Shizi street, Suzhou 215006, China*

[b]*College of Energy, Soochow University, 1 Shizi street, Suzhou 215006, China*

*Corresponding Author

E-mail: rlfan@suda.edu.cn

E-mail: mrshen@suda.edu.cn

Experimental section

Materials

Iron nitrate nonahydrate ($Fe(NO_3)_3•9H_2O$), sodium molybdenum oxide anhydrous (Na_2MoO_4), nickel sulfamate tetrahydrate ($Ni(NH_2SO_3)_2 • 4H_2O$), boric acid (H_3BO_3), ammonium citrate tribasic ($(NH_4)_3C_6H_5O_7$), sodium hydroxide (NaOH), potassium bicarbonate ($KHCO_3$), hydrochloric acid (HCl), sodium phosphate dibasic dehydrate ($Na_2HPO_4•2H_2O$) and sodium phosphate monobasic dihydydrate ($NaH_2PO_4•2H_2O$) were of analytical grade and used without further purification.

Fabrication of NiMoFe/Cu NWs electrodes

Firstly, the Cu foam substrate was cut into 1×1 cm^2, and then cleaned in 20% HCl solution to remove the surface oxides, followed by ultrasonically cleaned in ethanol and deionized water to remove the surface contaminants and dried in air. The electrochemical oxidation of the cleaned Cu foam to $Cu(OH)_2$ NWs was conducted in 1.0 M NaOH solution at a current density of 20 mA cm^{-2} for 20 minute. Afterward, the prepared $Cu(OH)_2$ NWs were calcined at 180℃ in the air for 2 h to obtain CuO NWs. The electrochemical reduction of CuO NWs to Cu NWs was conducted in Ar purged $KHCO_3$ solution at -1.4 V (vs. Ag/AgCl) for 10 minutes.

NiMoFe catalyst was integrated on Cu NWs *via* an electrodeposition method. The deposition solution consisted of 100 mM $Ni(NH_2SO_3)_2•4H_2O$, 2.5 mM Na_2MoO_4, 0.02M $(NH_4)_3C_6H_5O_7$, 0.5 M H_3BO_3 and various molar of $Fe(NO_3)_3•9H_2O$. Nitrogen was bubbled through the electrolyte solution for at least 15 min before deposition. The pH value of the deposition solution was adjusted to 4.5. A three-electrode configuration with a carbon rod, a saturated Ag/AgCl (3M KCl), and Cu NWs as the counter, reference, and working electrode, respectively, was used for the deposition process. Electrodeposition of NiMoFe on Cu NWs was performed for 120 s at a cathodic current density of -200 mA cm^{-2}. After electrodeposition, the sample was rinsed with deionized water and dried under vacuum at room temperature overnight. For comparison, NiFe/Cu NWs and NiMo/Cu NWs were synthesized along the same procedure without the addition of Na_2MoO_4 and $Fe(NO_3)_3•9H_2O$, respectively. NiMoFe Cu foam was

electrodeposited directly on the cleaned Cu foam for 120s at a cathodic current density of -200 mA cm^{-2}. After electrodeposition, these samples were rinsed with deionized water and dried under vacuum at room temperature overnight.

Materials characterizations

The surface morphology of the sample was analyzed using a field-emission scanning electron microscope (SEM) (SU8010, Hitachi). Transmission electron microscope (TEM) analysis was conducted by a JEOL 2100F operating at 200 kV. X-ray diffraction (XRD) was measured using an X-ray diffractometer in parallel beam mode with Cu Ka radiation (D/MAX-2000PC, Japanese Rigaku). X-ray photoelectron spectroscopy (XPS) measurements were performed at room temperature using a spectrometer hemispherical analyzer (ESCALAB 250Xi, Thermo). All the binding energies were referenced to adventitious carbon at 284.6 eV.

Electrochemical measurements

The electrochemical measurement was conducted in a three-electrode configuration with carbon rod as the counter electrode and Ag/AgCl (sat. KCl) as the reference electrode. The electrocatalysts were tested for the HER, OER and overall water splitting in a 1.0 M phosphate buffered saline (PBS) electrolyte(pH=6.5). The potentials are controlled using an electrochemical workstation (Vertex, Ivium Technologies) and re-scaled to the potential according to the following equation: $V_{RHE} = V_{Ag/AgCl} + 0.197\,V + pH \times 0.059\,V$. The HER and OER polarization curves were obtained at room temperature, with a scan rate of 2 mV s^{-1} to avoid the possible contribution of capacitive current. Before all the electrochemical measurements were performed, galvanostatic measurements at a fixed current density of -10 mA cm^{-2} or 10 mA cm^{-2} were performed until a stable potential was obtained. The Tafel slopes of different samples stemmed from their corresponding polarization curves. They can be calculated using the Tafel equation ($V_{op} = b\,log(J) + a$, where J, V_{op}, and b represent the current density, overpotential, and Tafel slope, respectively). Tafel plots were acquired by plotting the overpotentials versus the logarithm of the steady state current

densities.

Electrochemical impedance spectroscopy (EIS) measurements were performed by using an AC voltage with 5 mV amplitude in a frequency range from 0.1 Hz to 100 kHz in 1.0 M PBS solution at the potential of 1.8 V_{RHE}. The Nyquist plots were thus obtained based on the EIS data. The electrochemically active surface area (ECSA) was measured by CV in the potential windows 0.74-0.9 V_{RHE} where no faradaic reactions occurred, with different scan rates of 20, 40, 60, 80, 100, 120, 140, 160 and 200 mV s^{-1} by plotting the $\Delta J = (J_{anodic} - J_{cathodic})$ at 0.82 V_{RHE} against the scan rate. Chronopotentiometry tests were recorded at constant current with a current density of 10 mA cm^{-2} and 50 mA cm^{-2} for the HER and the OER in a 1.0 M PBS electrolyte without an iR-drop compensation, respectively.

For the overall water splitting measurements, using NiMoFe/Cu NWs as the anode and cathode, the performance of water electrolysis was characterized using polarization curves in a two-electrode configuration in 1.0 M PBS at a scan rate of 2 mV s^{-1} at room temperature. To evaluate the stability of NiMoFe/Cu NWs, long-term durability tests at a constant current density of 50 mA cm^{-2} were conducted in a 1.0 M PBS electrolyte solution. For the solar-driven water splitting, three series-connected ordinary Si solar cells were connected to NiMoFe/Cu NWs cathode and NiMoFe/Cu NWs anode to construct PV-electrolysis system. A 300 W Xe lamp (Oriel, Newport Co.) with a silica filter was used as a light source. Before the measurements, the light intensity was carefully controlled at 100 mW cm^{-2}, measured using an optical power meter (Newport Company) just before the light entered into the Si solar cells. The theoretical solar to hydrogen (STH) efficiency of PV-electrolysis system was calculated by the following equation.

$$STH\ effciency(\%) = \frac{I_{op}(mA\ cm^{-2}) \times 1.23(V) \times 100}{P_{solar}(mW\ cm^{-2})}$$

where, I_{op} is the operating current density of the PV-electrolysis system and P_{solar} is the power density of solar energy. The faradaic efficiency (FE) of overall water splitting was determined at a current density of 50 mA cm^{-2} for 5 h in 1.0 M PBS, and the amount

of gas produced on the overall water splitting system was obtained by using GC equipped with a thermal conductivity detector (Tianmei, GC 7900T). We recorded the amount of produced oxygen and hydrogen gas every 1 h. The faradaic efficiency of oxygen was calculated using the equation.

$$FE(\%) = n_{O_2} \times 4 \times F \div (i \times t) \times 100\%$$

where n_{O_2}represent the total amount of oxygen generated measured with GC during the overall water splitting, F stand for Faraday constant (96485 C mol^{-1}), and i and t represent the current (A) and reaction time (s), respectively. The calculation of hydrogen was similar to oxygen, expect that the coefficient is multiplied by 4 instead of 2.

Theoretical calculations

We used the Vienna ab initio simulation package (VASP) to perform the first-principles calculations.[1, 2] The interaction between the atomic cores and electrons were described according to the projector augmented wave (PAW), with the plane wave cutoff of 400 eV and spin polarization.[3] The semi-local exchange and correlation energies were described by the Generalized Gradient Approximation (GGA) with the Perdew–Burke–Ernzerhof (PBE) exchange–correlation functional.[4] The on-site Coulomb correlation was included within the GGA + U approach with an effective Hubbard U = 3, 6, 3 eV for Ni, Fe and Mo, respectively.[5] For the HER, a (3 × 3) Ni (111) surface with five layers was constructed, with the surface atom replaced with a Fe, or Mo atoms. For the OER, a (3 × 3) NiOOH supercell was constructed, with the Fe, or Mo atoms adsorbed on the surface. A 15 Å vacuum gap along the z-axis was adopted to eliminate the layer image interaction. A Monkhosrt-Pack grid 3 × 3 × 1 was used to carry out the calculations. The convergence criterion was set to 10^{-5} eV for total energies and 0.02 eV/Å for total forces. The Gibbs free energy change ΔG were evaluated by the formula[6, 7]:

$$\Delta G = \Delta E + \Delta ZPE - T\Delta S$$

where *E* is the total energy, ZPE is the zero-point energy, *T* is the temperature, and *S* is the entropy. The nudged elastic band (NEB) method was used to find the transition state in the water dissociation step in the HER.[8]

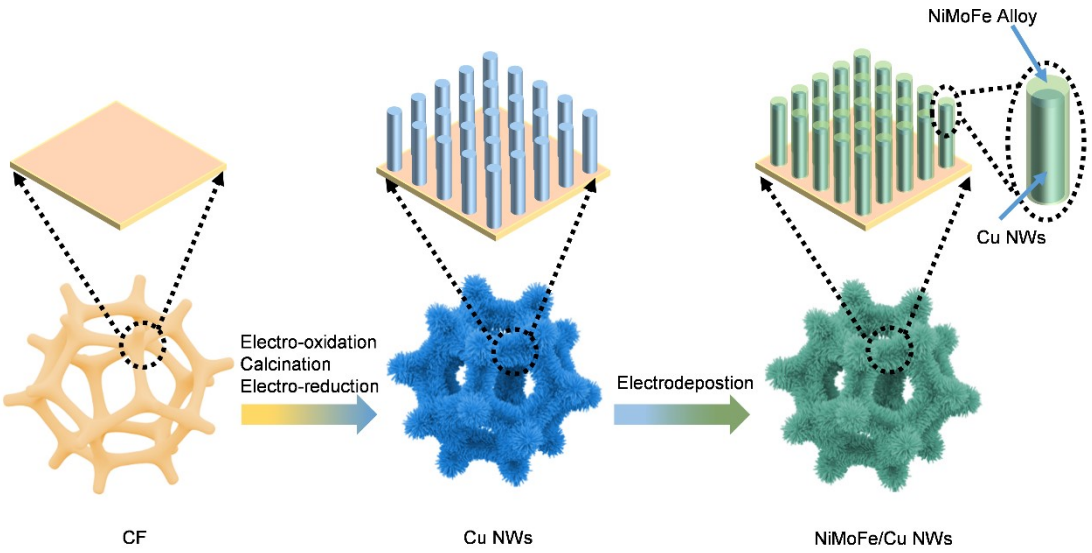

Fig. S1. Schematic illustration of the fabrication procedure for the NiMoFe/Cu NWs.

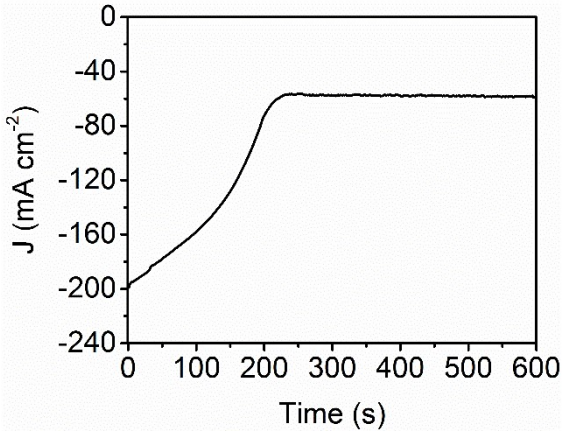

Fig. S2. The electrochemical reduction of CuO NWs to Cu NWs was conducted in Ar purged $KHCO_3$ solution at -1.4 V (vs. Ag/AgCl) for 10 minutes.

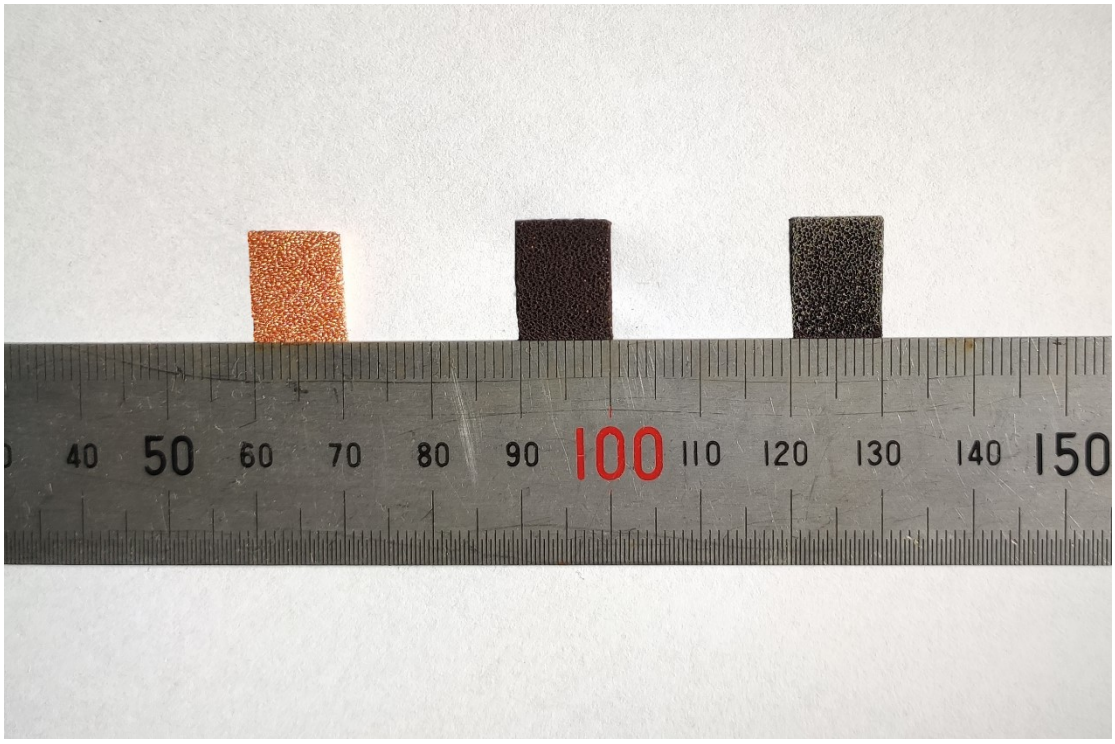

Fig. S3. Optical pictures of the CF, Cu NWs and NiMoFe/Cu NWs.

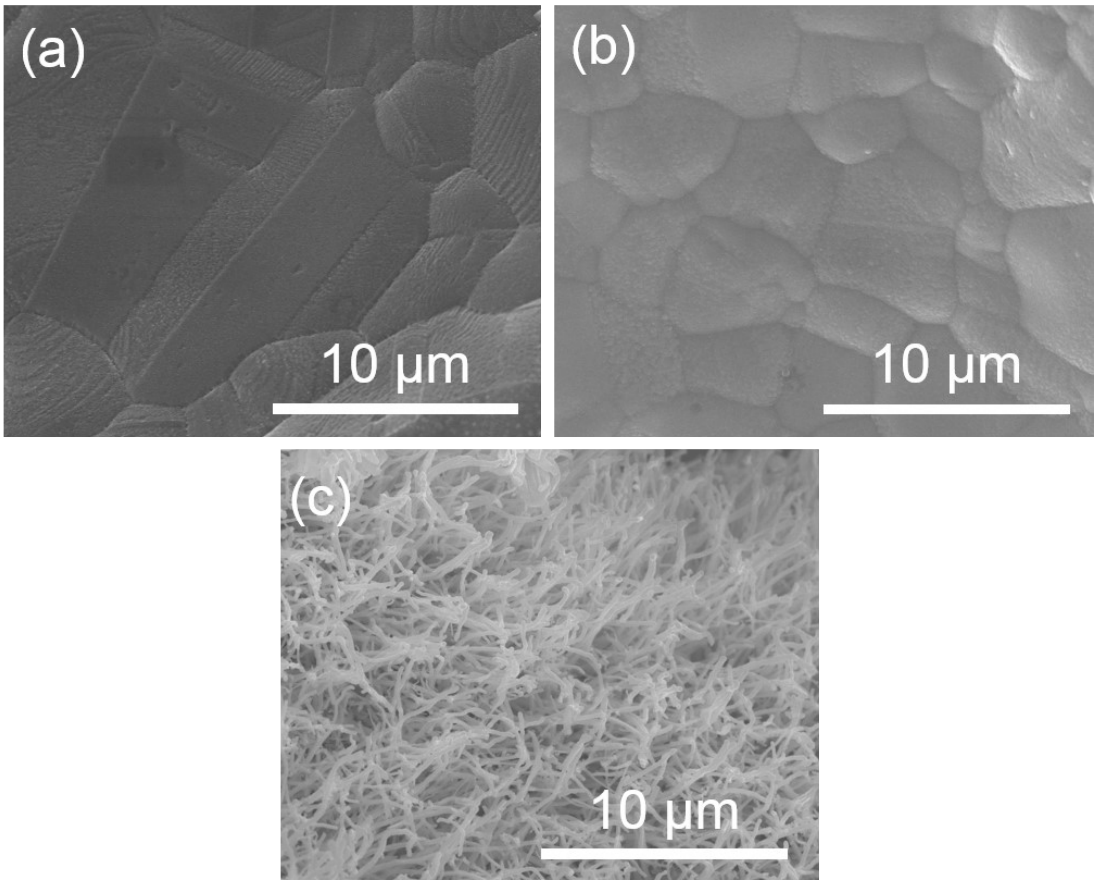

Fig. S4. SEM images of (a) CF, (b) NiMoFe/CF and (c) NiMoFe/Cu NWs.

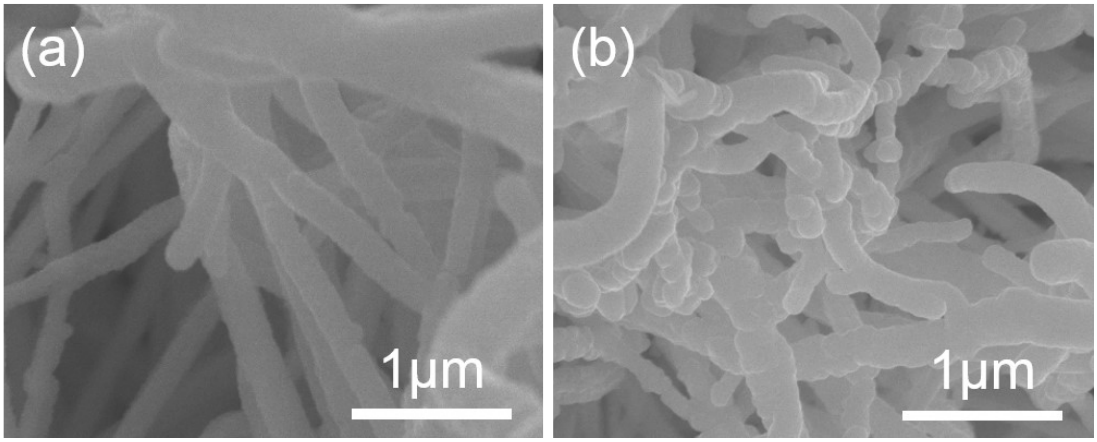

Fig. S5. SEM images of (a) NiMo/Cu NWs and (b) NiFe/Cu NWs.

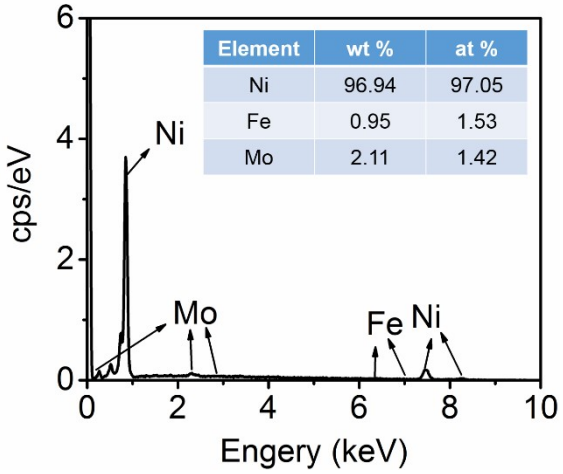

Fig. S6. EDX spectrum of NiMoFe/Cu NWs.

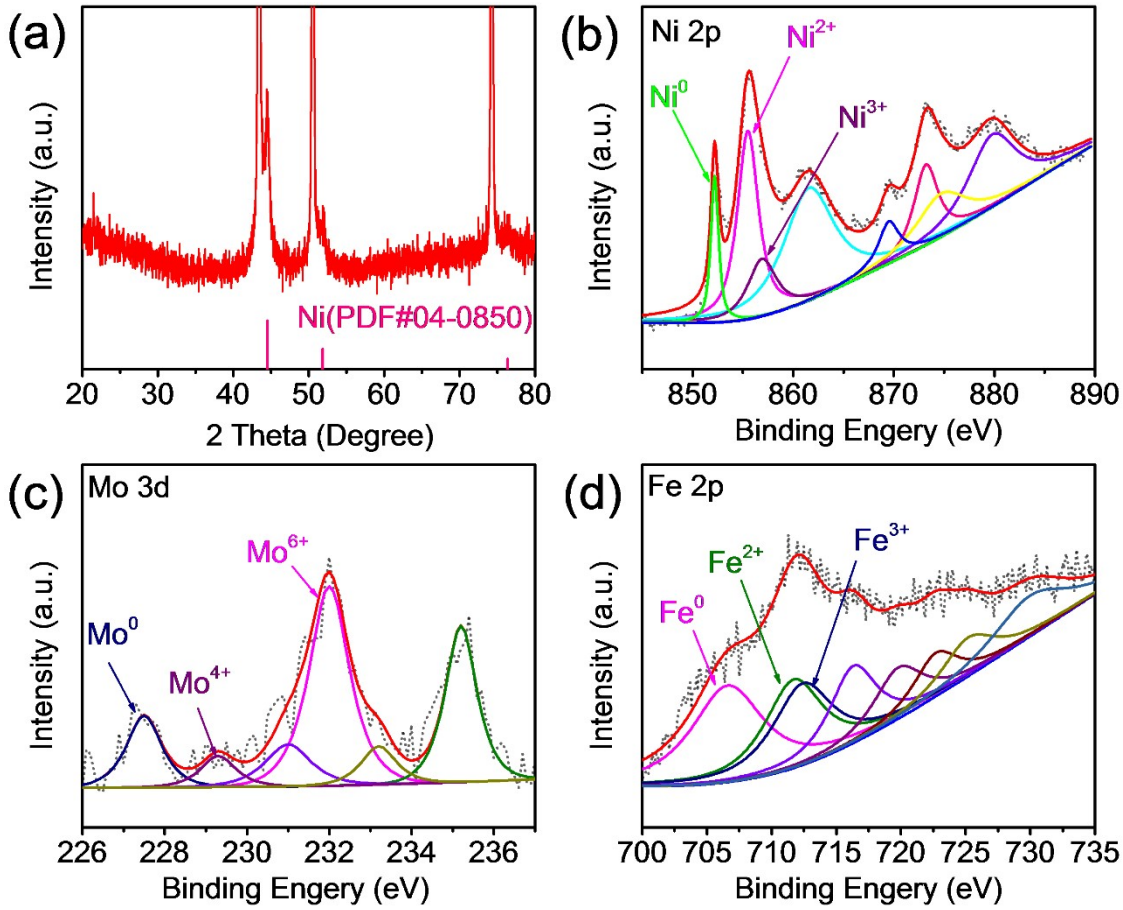

Fig. S7. (a) XRD patterns and high-resolution XPS: (b) Ni 2p, (c) Mo 3d and (d) Fe 2p spectra of the NiMoFe/Cu NWs sample.

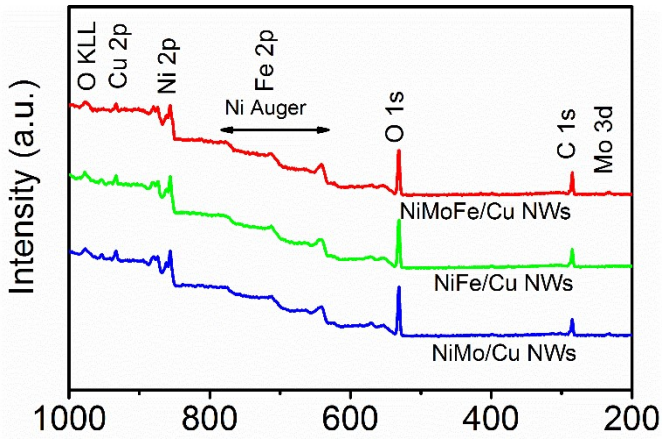

Fig. S8. The survey XPS spectra of NiMoFe/Cu NWs, NiFe/Cu NWs and NiMo/Cu NWs.

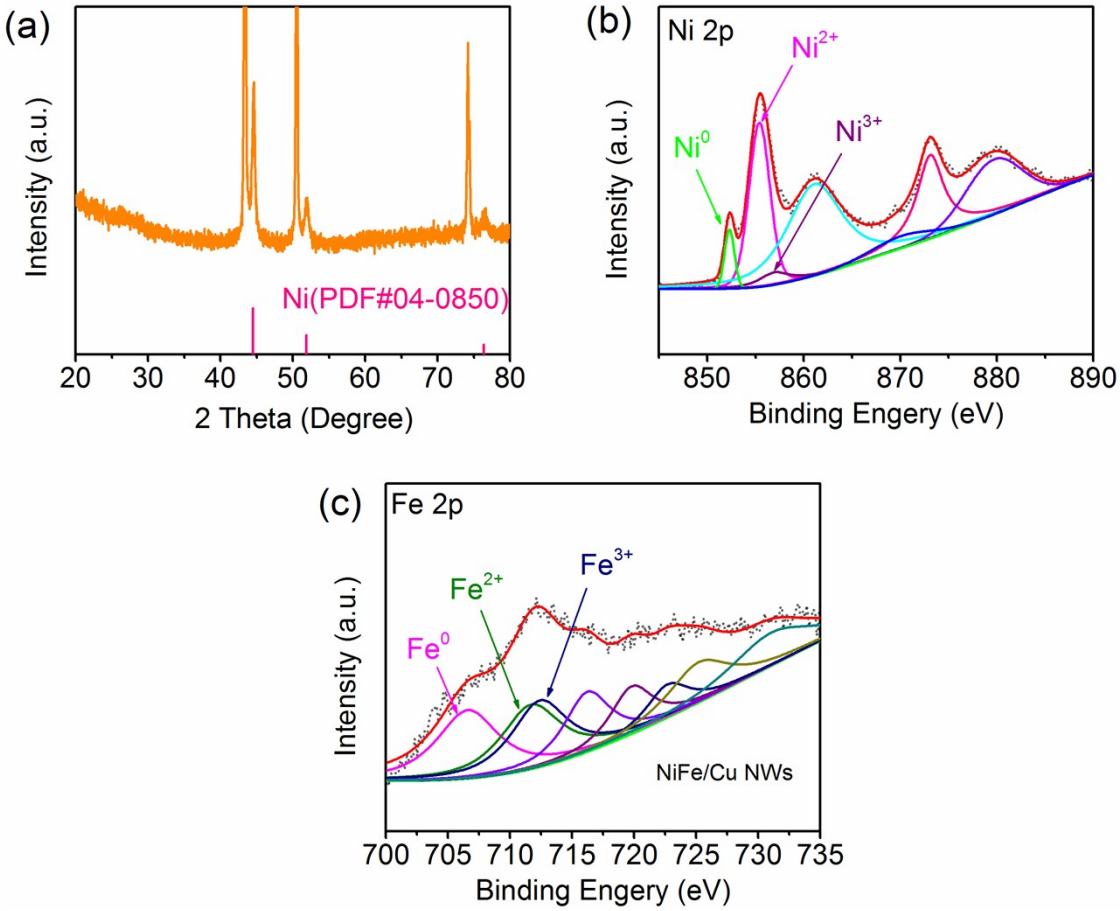

Fig. S9. (a) XRD patterns and high-resolution XPS: (b) Ni 2p and (c) Fe 2p spectra of the NiFe/Cu NWs sample.

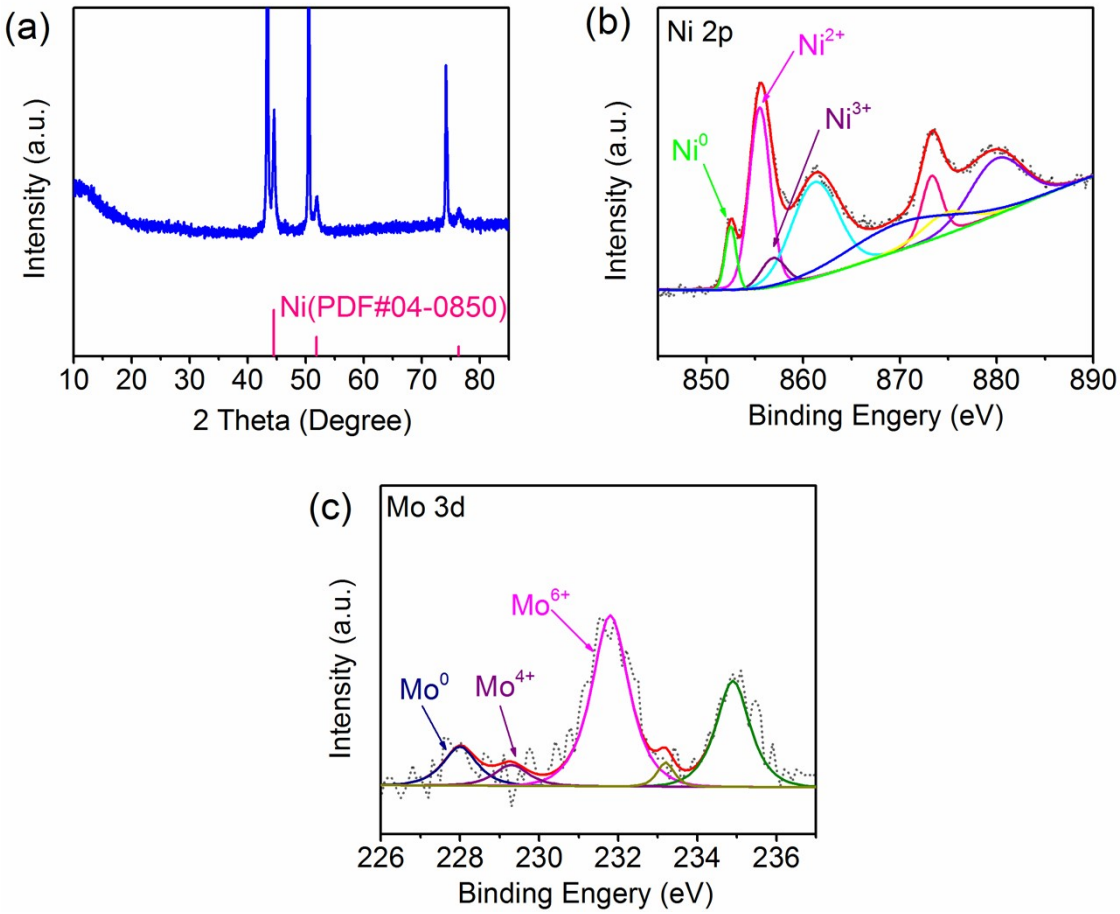

Fig. S10. (a) XRD patterns and high-resolution XPS: (b) Ni 2p and (c) Mo 3d spectra of the NiMo/Cu NWs sample.

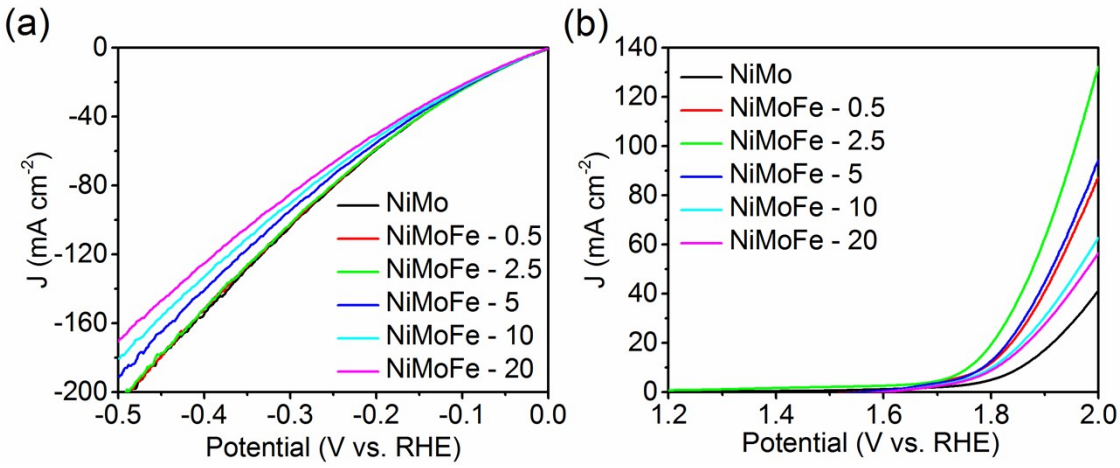

Fig. S11. Polarization curves for (a) HER and (b) OER of the NiMoFe - x (x=0, 0.5, 2.5, 5, 10, 20) in 1.0 M PBS.

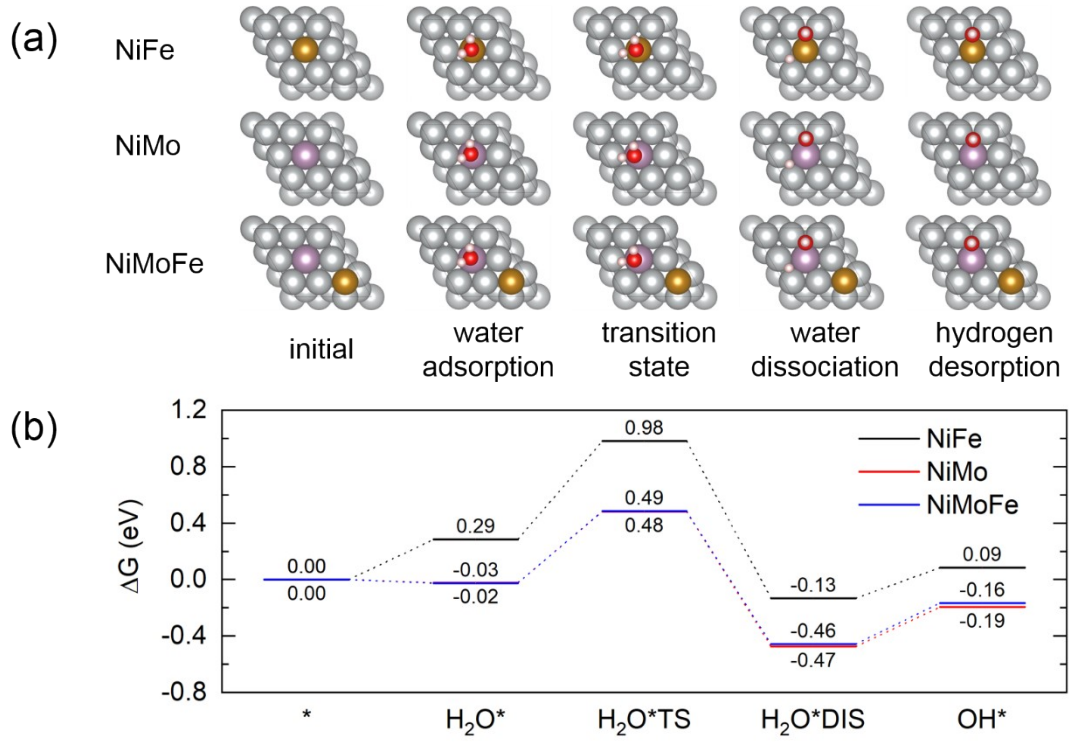

Fig. S12. Theoretical calculation of HER energy profile over NiFe, NiMo and NiMoFe catalysts. (a) Binding configurations for NiFe, NiMo and NiMoFe surfaces at different stages on the reaction path. (b) Gibbs free energy profiles for HER on NiFe, NiMo and NiMoFe surfaces.

Generally, water dissociation and hydrogen desorption on the surface of the catalyst are known as the key factors for neutral HER. Among all of the three catalysts investigated, water dissociation was found to be the rate-determining step. Compared to the NiFe surface, the activation energy of water dissociation on the NiMo and NiMoFe surfaces was significantly reduced from 0.69 to 0.50 and 0.52 eV, suggesting a superior water dissociation capability. Therefore, it can be concluded that Mo species played an important role in reducing the activation energy of water dissociation and thus accelerated the overall HER kinetics.

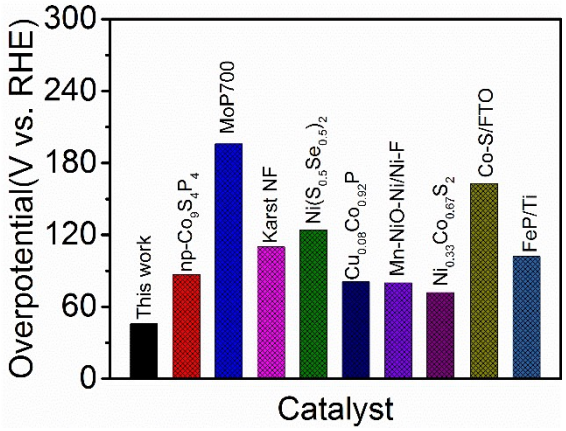

Fig. S13. Comparison of the HER performance of NiMoFe/Cu NWs with other recently reported electrocatalysts in 1.0 M PBS.

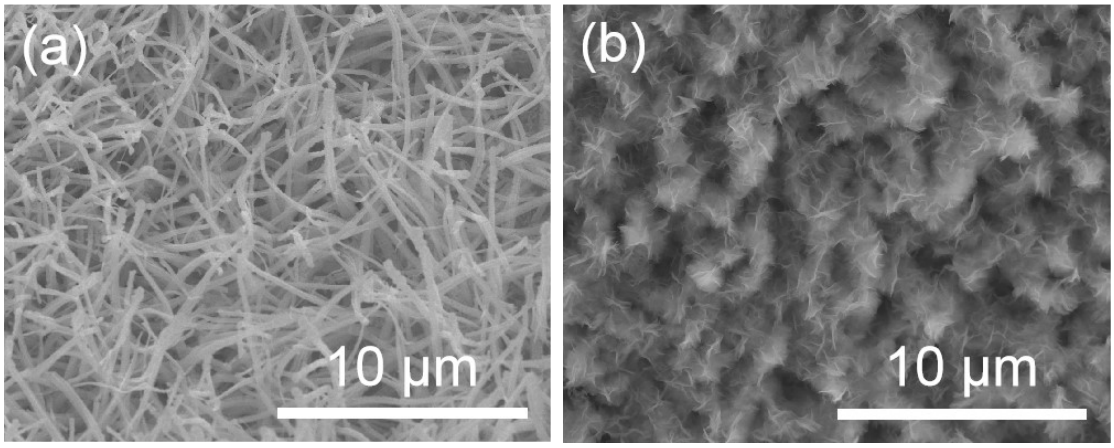

Fig. S14. SEM images of NiFeMo/Cu NWs after long-term stability test over 48 h toward (a) HER and (b) OER.

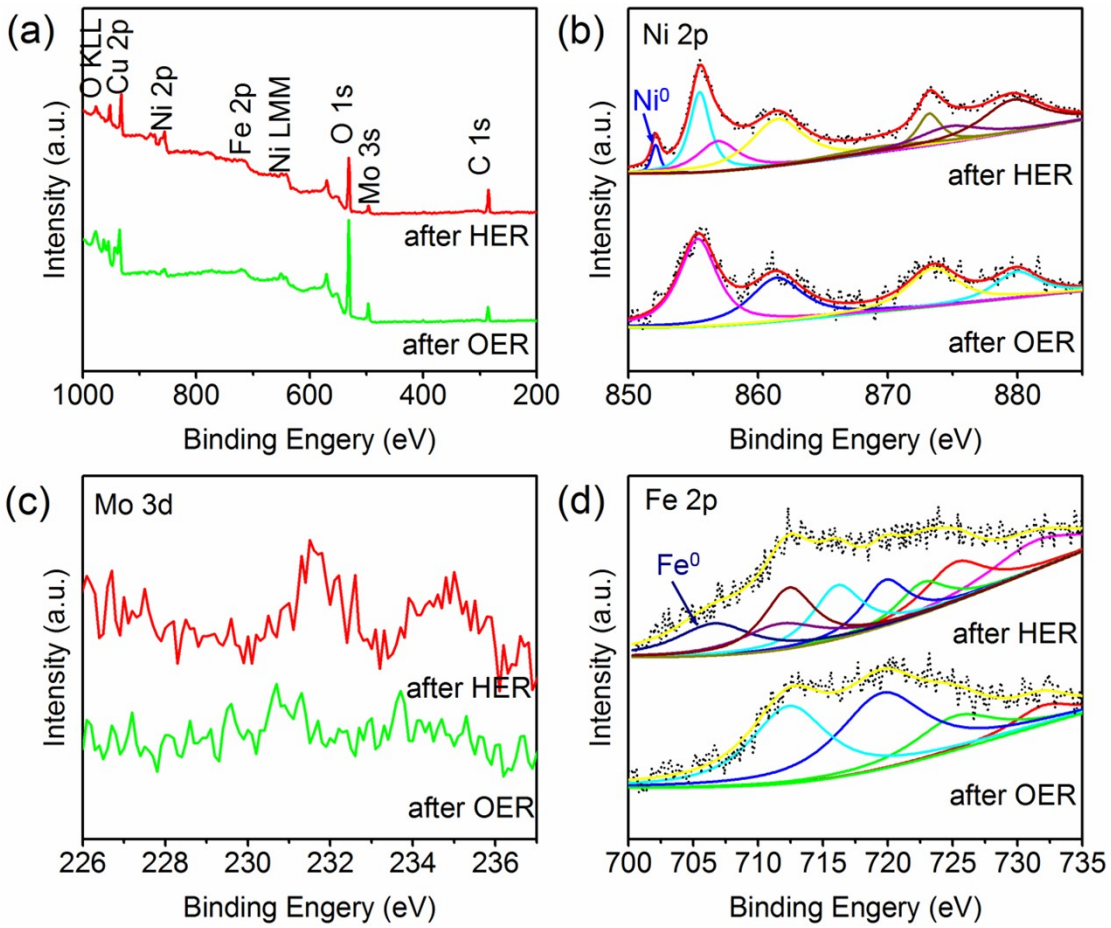

Fig. S15. Comparison XPS spectra of NiMoFe/Cu NWs after HER and OER : (a) full survey, (b) Ni 2p, (c) Mo 3d and (d) Fe 2p.

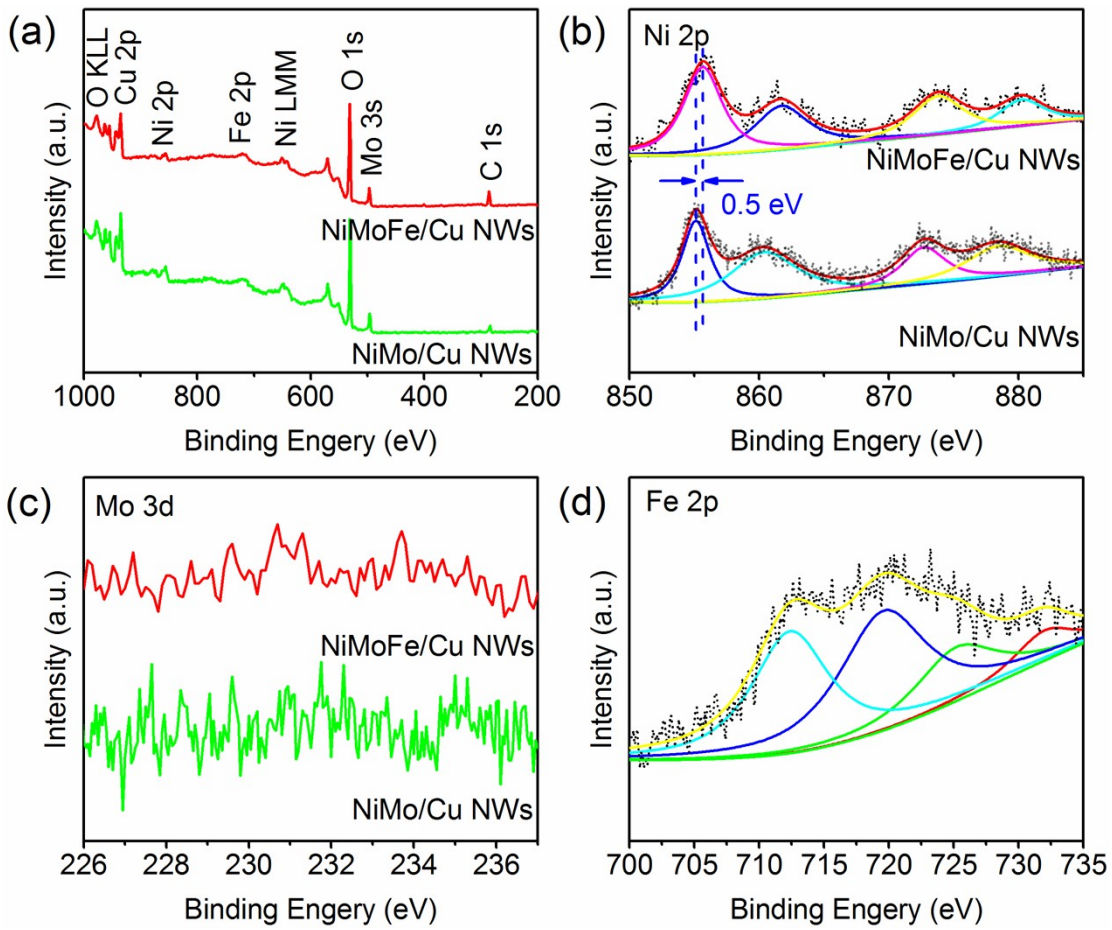

Fig. S16. High-resolution XPS of Ni 2p after NiMoFe/Cu NWs and NiMo/Cu NWs perform OER test.

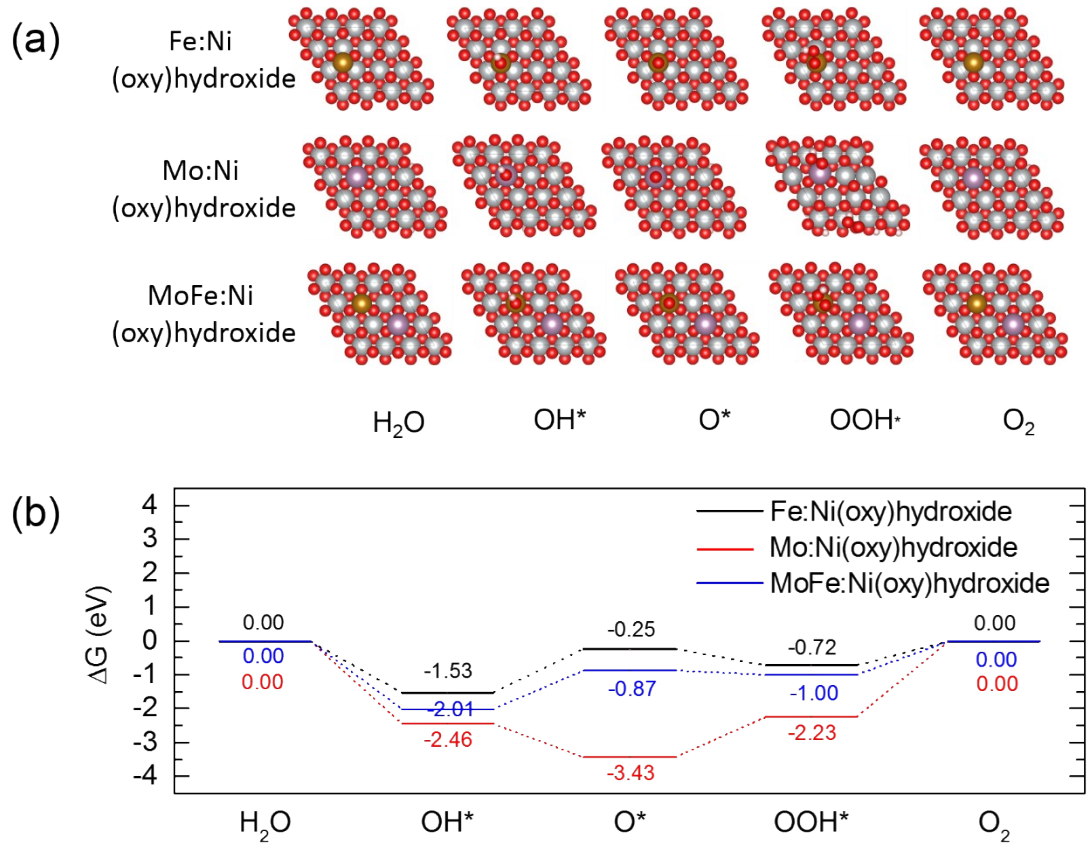

Fig. S17. (a) The proposed 4e-mechanism and (b) corresponding Gibbs free energy diagram for OER of the Fe:Ni (oxy)hydroxide, Mo:Ni (oxy)hydroxide and MoFe:Ni (oxy)hydroxide.

In the case of OER, the widely accepted pathway involves a four-step proton−electron transfer with the formation of *OH, *O, and *OOH intermediates (where * indicates the active site of catalyst).[9,10] It is generally believed that the surface of Ni based alloys can be easily oxidized to the Ni (oxy)hydroxide in the aqueous and strongly oxidative environments of OER, and Ni (oxy)hydroxide was popularly regarded as the active species for OER.[11-14] Fig. S16 shows the proposed 4e-mechanism and corresponding Gibbs free energy diagram for OER of the Fe:Ni (oxy)hydroxide, Mo:Ni (oxy)hydroxide and MoFe:Ni (oxy)hydroxide. The OER activity Fe:Ni (oxy)hydroxide was determined by the free energy change in the *O formation (2.51 eV), which is much lower than the free energy change in the rate-determining step for the Mo:Ni (oxy)hydroxide (3.46 eV), suggesting that Fe doping was more prominent than the Mo doping in boosting the OER activity of the Ni (oxy)hydroxide. Similar with

that of the Fe:Ni (oxy)hydroxide, *O formation is also the rate-determining step of OER for the MoFe:Ni (oxy)hydroxide. Specifically, the free energy change in the rate-determining step for MoFe:Ni (oxy)hydroxide (2.37) was significantly lower than that for the Fe:Ni (oxy)hydroxide (2.51 eV) and Mo:Ni (oxy)hydroxide (3.46 eV), indicating that Fe and Mo dual doping was a synergistic effect to increase the OER activity of Ni (oxy)hydroxide. These DFT calculations agreed well with our experimental results that Fe played a leading part, and Fe and Mo worked synergistically on the OER activity of NiMoFe (oxy)hydroxide.

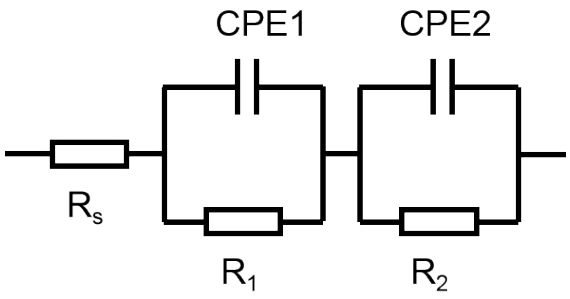

Fig. S18. The equivalent circuit of catalysts.

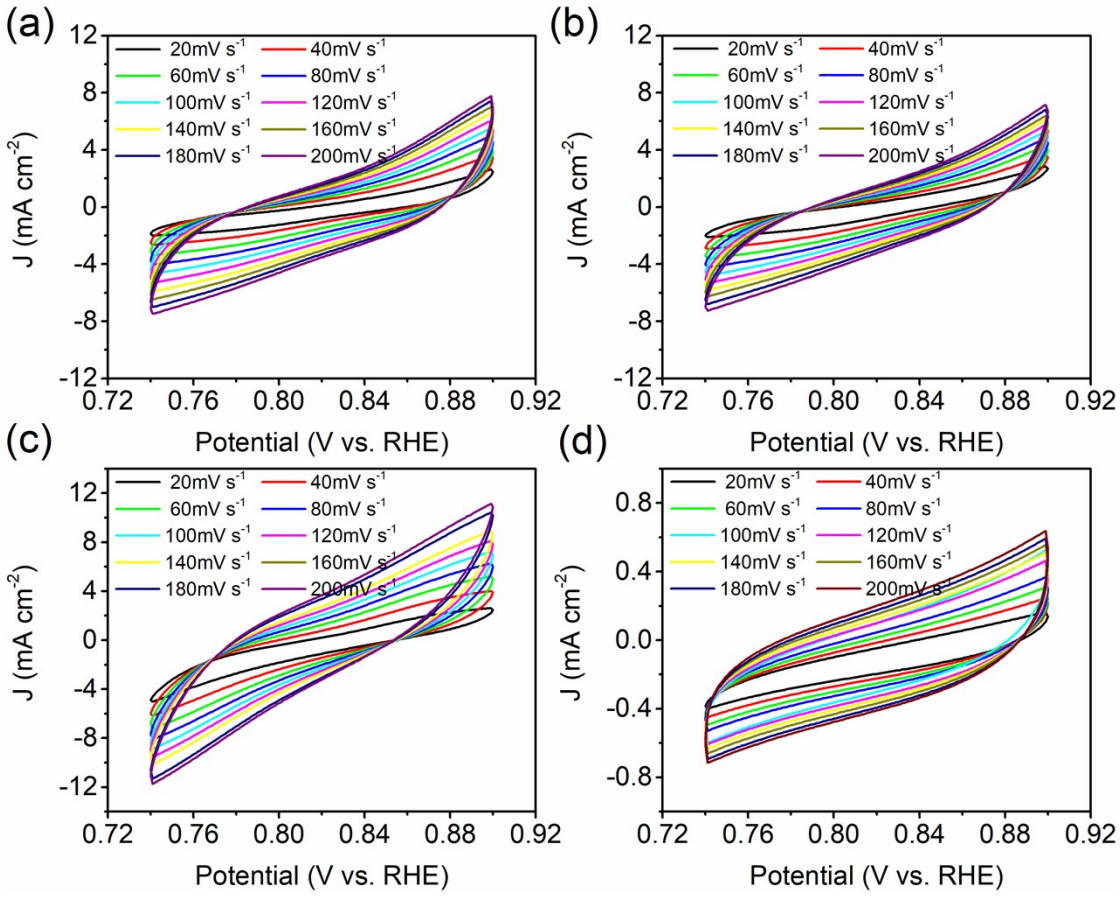

Fig. S19. Cyclic voltammograms of (a) NiFeMo/Cu NWs, (b) NiFe/Cu NWs, (c) NiMo/Cu NWs and (d) NiFeMo/CF in 1.0 M PBS at various scanning rates (from 20 to 200 mV s^{-1}), within a potential range from 0.74 to 0.90 V vs. RHE.

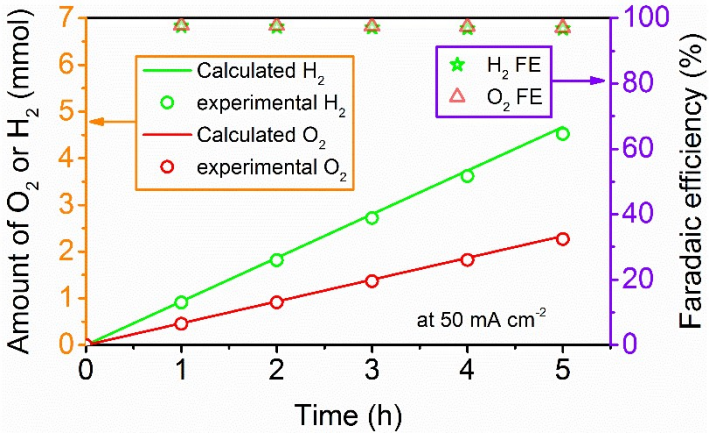

Fig. S20. Calculated and experimental H_2 and O_2 production, and the HER and OER Faradic efficiency for NiMoFe/Cu NWs electrode as the function of time at a constant current density of 50 mA cm^{-2} during overall water splitting.

Table S1. The summary of catalytic performances and stability of electrocatalysts for overall water splitting in neutral media.

Catalysts	Cell voltage at 10mA cm^{-2} (V)	pH, electrolyze	Stability(h)	Ref.
NiMoFe/NWs	1.82 V	pH = 6.5, 1 M PBS	50 mA, 48 h	This work
Fe@Fe_xNiO/Ni @Ni_yCoP	1.86 V	pH = 7, 1 M PBS	100 mA, 100 h	J. Mater. Chem. A 2021, 9, 13562-13569.
CoP/CeO_2-FeO_xH	1.82 V	pH = -, 1 M PBS	50 mA, 60 h	ACS Sustain. Chem. Eng. 2021, 9, 11981-11990.
NCS/NS-rGO	1.91 V	pH = 7.4, 1 M PBS	10 mA, 10 h	Nano Res. 2021, 14, https://doi.org/10.1007/s12274-021-3580-z.
$Ni(S_{0.5}Se_{0.5})_2$	1.87 V	pH = 7, 1 M PBS	10 mA, 12 h	J. Mater. Chem. A 2019, 7, 16793-16802.
Mn-FeP/$Co_3(PO_4)_2$	1.82 V	pH = 7, 1 M PBS	5 mA, 8 h	ChemSusChem 2019, 12, 1334-1341.
Co-Mo_2C@NC	1.83 V	pH = 7, 0.2 M PBS	10 mA, 11 h	J. Colloid Interface Sci. 2018, 532, 774-781
$Ni_{0.1}Co_{0.9}P$/CP	1.89 V	pH = 7, 1 M PBS	10 mA, 20 h	Angew. Chem. Int. Ed. 2018, 57, 15445-15449
S-$NiFe_2O_4$/NF	1.95 V	pH = 7.4, 1 M PBS	10 mA, 24 h	Nano Energy 2017, 40, 264-273.
Ni_3N@Ni-Bi NS/Ti	1.95 V	pH = 9.2, 0.5 M K-Bi	10 mA, 20 h	J. Mater. Chem. A, 2017, 5, 15445-15449.
CoP NA/CC	1.91 V	pH = 7, 1 M PBS	10 mA, 36 h	ChemElectroChem 2017, 4, 1840-1845.
NiP_2/CC	~2.16 V	pH = 7, 1 M PBS	-, 5 h	New J. Chem. 2017, 41, 2154-2159.
CoO/$CoSe_2$	2.18 V	pH = 6.5, 0.5 M PBS	10 mA, 10 h	Adv. Sci. 2016, 3, 1500426.
N, P, O-doped	1.92 V	pH = 7,	2 mA,	Energy Environ. Sci.

graphite	0.2 M PBS	10 h	2016, 9, 1210-1214.

Table S2. A summary of our photovoltaic-electrolysis water splitting performance and various reported water electrolysis cells for water splitting.

Water electrolysis cell	PV cells	η_{STE}	Electrlyte	η_{ETH}	η_{STH}	Ref.
NiMoFe/Cu NWs	three series-connected Si solar cells	20.3%	1 M PBS	54.1%	10.99%	This work
NSF/CNT	a commercial Si PV module connected to the as-designed two-cell electrolyser	14.4%	1 M KOH	72.2%	10.4%	J. Mater. Chem. A 2020,8, 16609-16615.
karst NF	a commercial planar silicon solar cell	25.5%	Seawater	64.7%	16.5%	Energy Environ. Sci. 2020, 13, 174-182
Mo/Ni/n^+np^+-Si	2 SC Si PV cells	13.5%	1 M NaOH	68.9%	9.3%	J. Mater. Chem. A 2019, 7, 2200-2209.
CoP	a 2-piece, series connected crystalline Si solar cell	-	1 M NaOH	-	5.3%	J. Mater. Chem. A 2018, 6, 1266-1274
Ni−Co−S/Ni−Co−P	3 series-connected c-Si PV cells	14.4%	1 M NaOH	77.1%	11.1%	J. Mater. Chem. A 2018, 6, 20297-20303.
NiFeSP/NF	a Si solar cell	28.5%	1 M KOH	32.3%	9.2%	ACS Nano 2017, 11, 10303-10312.
NiFe/Ni	four series-connected Si heterojunction (SHJ) solar cells	14.49 %	1 M NaOH	65.8%	9.54%	Nano Energy 2017, 42, 1-7.
Ni-NPs@NC	a commercial	-	1 M KOH	-	10.6%	ACS Appl.

	polycrystalline solar cell					Mater. Interfaces 2016, 8, 35390-35397.
CoMnO@CN	a commercial planar Si solar cell	16.1%	1 M KOH	49.7%	8%	J. Am. Chem. Soc. 2015, 137, 14305-14312.
NiFe LDH	two perovskite solar cells connected in series as a tandem cell	17.3%	1 M NaOH	71.1%	12.3%	Science, 2014, 345, 1593-1596.

η_{STE}: solar-to-electric conversion efficiency; η_{STH}: solar-to-hydrogen conversion efficiency; η_{ETH}: electric-to-hydrogen conversion efficiency;

1.G. Kresse and J. Furthmüller, *Phys. Rev. B.*, 1996, **54**, 11169-11186.

2.G. Kresse and J. Furthmüller, *Comput. Mater. Sci.*, 1996, **6**, 15-50.

3.G. Kresse and D. Joubert, *Phys. Rev. B.*, 1999, **59**, 1758-1775.

4.J. P. Perdew, K. Burke and M. Ernzerhof, *Phys. Rev. Lett.*, 1996, **77**, 3865-3868.

5.S. L. Dudarev, G. A. Botton, S. Y. Savrasov, C. J. Humphreys and A. P. Sutton, *Phys. Rev. B.*, 1998, **57**, 1505-1509.

6.J. K. Nørskov, T. Bligaard, A. Logadottir, J. R. Kitchin, J. G. Chen, S. Pandelov and U. Stimming, J. Electrochem. Soc., 2005, **152**, J23.

7.J. K. Nørskov, J. Rossmeisl, A. Logadottir, L. Lindqvist, J. R. Kitchin, T. Bligaard and H. Jónsson, *J. Phys. Chem. B.*, 2004, **108**, 17886-17892.

8.T. D. Kuhne, M. Iannuzzi, M. Del Ben, V. V. Rybkin, P. Seewald, F. Stein, T. Laino, R. Z. Khaliullin, O. Schutt, F. Schiffmann, D. Golze, J. Wilhelm, S. Chulkov, M. H. Bani-Hashemian, V. Weber, U. Borstnik, M. Taillefumier, A. S. Jakobovits, A. Lazzaro, H. Pabst, T. Muller, R. Schade, M. Guidon, S. Andermatt, N. Holmberg, G. K. Schenter, A. Hehn, A. Bussy, F. Belleflamme, G. Tabacchi, A. Gloss, M. Lass, I. Bethune, C. J. Mundy, C. Plessl, M. Watkins, J. VandeVondele, M. Krack and J. Hutter, *J. Chem. Phys.*, 2020, **152**, 194103.

9.V. Vij, S. Sultan, A. M. Harzandi, A. Meena, J. N. Tiwari, W.-G. Lee, T. Yoon and K. S. Kim, *ACS Catal.*, 2017, **7**, 7196-7225.

10.P. Li, X. Duan, Y. Kuang, Y. Li, G. Zhang, W. Liu and X. Sun, *Adv. Energy Mater.*, 2018, **8**, 1703341.

11.M. W. Louie and A. T. Bell, *J. Am. Chem. Soc.*, 2013, **135**, 12329-12337.

12.L. Trotochaud, S. L. Young, J. K. Ranney and S. W. Boettcher, *J Am Chem Soc*, 2014, **136**, 6744-6753.

13. S. Jin, *ACS Energy Lett.*, 2017, **2**, 1937-1938.

14.M. Han, N. Wang, B. Zhang, Y. Xia, J. Li, J. Han, K. Yao, C. Gao, C. He, Y. Liu, Z. Wang, A. Seifitokaldani, X. Sun and H. Liang, *ACS Catal.*, 2020, **10**, 9725-9734.